



**HAL**  
open science

## Partitioning of Solutes at Crystal Defects in Borides After Creep and Annealing in a Polycrystalline Superalloy

Lola Lilensten, Aleksander Kostka, Sylvie Lartigue-Korinek, Baptiste Gault,  
Sammy Tin, Stoichko Antonov, Paraskevas Kontis

► **To cite this version:**

Lola Lilensten, Aleksander Kostka, Sylvie Lartigue-Korinek, Baptiste Gault, Sammy Tin, et al.. Partitioning of Solutes at Crystal Defects in Borides After Creep and Annealing in a Polycrystalline Superalloy. JOM Journal of the Minerals, Metals and Materials Society, 2021, 73, pp.2293-2302. 10.1007/s11837-021-04736-5 . hal-03435740

**HAL Id: hal-03435740**

**<https://hal.science/hal-03435740>**

Submitted on 18 Nov 2021

**HAL** is a multi-disciplinary open access archive for the deposit and dissemination of scientific research documents, whether they are published or not. The documents may come from teaching and research institutions in France or abroad, or from public or private research centers.

L'archive ouverte pluridisciplinaire **HAL**, est destinée au dépôt et à la diffusion de documents scientifiques de niveau recherche, publiés ou non, émanant des établissements d'enseignement et de recherche français ou étrangers, des laboratoires publics ou privés.

# Partitioning of solutes at crystal defects in borides after creep and annealing in a polycrystalline superalloy

Lola Lilensten<sup>1, #, \*</sup>, Aleksander Kostka<sup>2</sup>, Sylvie Lartigue-Korinek<sup>3</sup>, Baptiste Gault<sup>1, 4</sup>, Sammy Tin<sup>5</sup>, Stoichko Antonov<sup>1</sup>, Paraskevas Kontis<sup>1, \*</sup>

<sup>1</sup> Max-Planck-Institut für Eisenforschung, Max-Planck Straße 1, 40237 Düsseldorf, Germany

<sup>2</sup> Center for Interface-Dominated High Performance Materials (ZGH), Ruhr-Universität 44801, Bochum, Germany

<sup>3</sup> Institut de Chimie et des Matériaux Paris Est, UMR CNRS UPEC 7182, F-94320 Thiais, France

<sup>4</sup> Department of Materials, Imperial College, South Kensington, London SW7 2AZ, UK

<sup>5</sup> Illinois Institute of Technology, 10 W. 32nd Street, Chicago, IL, 60616, USA

<sup>#</sup> Now at PSL Research University, Chimie ParisTech, Institut de Recherche de Chimie Paris, CNRS UMR 8247, Paris, France

<sup>\*</sup> Corresponding authors: [lola.lilensten@chimieparistech.psl.eu](mailto:lola.lilensten@chimieparistech.psl.eu), [p.kontis@mpie.de](mailto:p.kontis@mpie.de)

This is a post-peer-review, pre-copyedit version of an article published in JOM. The final authenticated version is available online at: <https://doi.org/10.1007/s11837-021-04736-5>

## Abstract

We have investigated the partitioning of solutes at crystal defects in intergranular Cr-rich  $M_2B$  borides after creep at 850°C/185MPa and annealing at 850°C for approximately 3000 hours in a polycrystalline nickel-based superalloy. Borides were found to coarsen in both cases, with the borides after creep to be the thickest (800-1100nm), compared to borides annealed in the absence of external applied load (400-600nm). Transmission electron microscopy revealed that the coarsened borides have either a tetragonal  $I4/mcm$  structure, or an orthorhombic  $Fddd$ , with those two structures coexisting in a single particle. The presence of a very high density of planar faults is systematically

observed within the coarsened borides. The faults were correlated with chemical fluctuations of B and Cr, revealed by atom probe tomography. In addition, partitioning of Ni and Co was observed at dislocations within the borides after creep providing insights into the deformation of borides.

## **Keywords**

Boride, faulted planes, dislocations, coarsening, solute partitioning

### **1. Introduction**

Boron, although it is considered a minor elemental addition in both nickel- and cobalt-based superalloys, it has major consequences on their microstructure and mechanical performance [1,2]. It is well documented that boron is typically found at grain boundaries, either segregated as an element in solid solution [3,4] or precipitated in the form of various borides, such as  $M_2B$ ,  $M_5B_3$  or  $M_3B_2$  [2,5–10]. In the former case, it was suggested that interfacial boron increases the strength and cohesion of the grain boundary [11,12], thereby contributing to an overall ductility enhancement. However, in the latter case, borides have a contradicting character. In some cases, borides were found to be beneficial to the mechanical performance under creep conditions [13–15], whereas in other cases they act as dislocations sources that facilitate micro-crack initiation and micro-twinning under creep [1,16–18].

Many studies focused mainly on the composition of borides prior to deformation [5,9,19,20] or after creep of the alloy [15]. Yet, they do not provide insights into the microstructural evolution of intergranular borides, such as coarsening or dissolution, when subjected to thermal exposure with or without applied load. In addition, the deformation behavior of borides under creep at the near-atomic level, and the possible interaction of solutes with crystal defects, that become an important alloy design parameter [21,22], have not yet been explored. Thus, a deeper understanding of the microstructural evolution of the borides under creep is required to evaluate their role on the mechanical performance of polycrystalline superalloys.

In this study, the polycrystalline nickel-based superalloy STAL15-CC was crept at 850°C under 185MPa load up to fracture (time to fracture approximately 3000 hours). We investigated the microstructural evolution of the intergranular Cr-rich  $M_2B$  borides after deformation at 850°C that evolves the presence of planar faults within the coarsened borides. In order to determine a possible role of the external applied stress on the borides evolution, samples of STAL15-CC were statically annealed at 850°C, i.e. in the absence of any externally applied load, for an equivalent time to the creep rupture time (i.e. 3000 hours), and compared to the initial and the crept specimens.

Our findings allow us to investigate the microstructural evolution and solutes partitioning behavior of borides under thermal exposure at 850°C, with a focus on the interaction between solutes and crystal defects occurring in these precipitates. This provides new insights into the microstructural evolution of borides and hence improves the current understanding of borides and their role on the mechanical performance of polycrystalline superalloys.

## **2. Materials and methods**

The polycrystalline nickel-based STAL15-CC superalloy used in this study has a nominal composition of Ni-16.50Cr-5.50Co-0.60Mo-1.20W-10.00Al-2.40Ta-0.02Hf-0.5C-0.05B-0.01Zr (at.%). Following vacuum investment casting, specimens were hot isostatically pressed at 1150°C for 5 h under a pressure of 175 MPa to minimize internal casting porosity. This was followed by a solution heat-treatment at 1120°C for 4 h, air cooled, and further aging heat treated at 845°C for 24 h followed by air cooling. Creep specimens were machined from fully heat-treated bars, with a gauge length of 25mm and tested at 850°C/185 MPa up to fracture. Samples from fully heat-treated bars were annealed at 850°C for 3000 hours, and air-cooled. The annealing time was selected based on the corresponding creep rupture time for creep at 850°C and 185 MPa, which was approximately 3000 hours. Hereafter this sample is referred to simply as annealed.

The crept specimens were cut along the load axis and then polished with abrasive media down to 0.04µm colloidal silica surface finish. Same surface preparation was followed for the annealed samples. Backscattered electron (BSE) micrographs were recorded on a Zeiss Merlin scanning electron microscope (SEM) at an accelerating voltage of 20 kV and a probe current of 2 nA.

Specimens for transmission electron microscopy (TEM) were prepared from both crept and annealed samples using a FEI Helios Nanolab G4 CX focused ion beam system (FIB) operated at 30 kV. Low, 5 kV ion beam cleaning was applied for 2 minutes to each side of the TEM lamella in order to remove FIB beam damage. TEM imaging and diffraction were performed using a FEI Tecnai Supertwin F20 operated at 200 kV and equipped with a high angle annular dark-field (HAADF) detector. Atomic resolution image simulations were calculated using the MacTempas software using multislice calculation [23]. The atomic structure is built using the Crystal Kit software and it is superimposed to the simulation [23].

Atom probe tomography (APT) specimens were prepared using a dual beam SEM/FIB instrument (FEI Helios Nanolab 600) via a site-specific lift-out protocol and mounted on a Si coupon [24]. Coarsened borides at grain boundaries were identified by backscattered imaging and targeted for the

lift-out process, in order to collect compositional information from these particular particles. APT measurements were carried out on a Cameca LEAP<sup>TM</sup> 5000 HR operated in laser pulsing mode at a pulse repetition rate of 125 kHz and a pulse energy of 55 pJ. The base temperature was set to 60K and the detection rate was maintained at 15 ions every 1000 pulses. Data analyses were performed using the IVAS 3.8.2 software package.

### 3. Results and discussion

#### 3.1. Coarsening of borides under creep and annealing at 850°C

Figure 1 shows intergranular borides in the STAL15-CC alloy in different microstructural states. Figure 1a shows a grain boundary after full heat treatment. The grain size is approximately 750  $\mu\text{m}$ , and a  $\gamma'$  volume fraction of 51.8% is calculated in this alloy by the lever rule (see Figure S1 in the supplementary material) [25]. Although the lever rule applies to dual-phase  $\gamma/\gamma'$  microstructures, the amount of grain boundary precipitation in the present alloy is believed to be negligible enough to not influence significantly the calculation of the  $\gamma'$  volume fraction, especially for the heat-treated state considered for the calculation. The dark contrast Cr-rich borides can be more clearly seen in the close-up in Figure 1b, alongside MC carbides and large grain boundary  $\gamma'$  precipitates [2,15]. As shown in Figure 1b the borides are rather small. Measurements performed on 145 borides in the heat-treated condition led to an average size of  $210\pm 80$  nm. Results on this alloy's heat-treated state can be found in the literature [2,14,15].

Figure 1c shows a grain boundary and the borides after creep at 850°C, revealing microstructural alterations. In particular, the size of the borides has increased substantially, to  $1060\pm 340$  nm (measurements performed on 74 borides). In order to separate the contributions of the deformation and that of the heat treatment seen by the sample during the creep test, a sample annealed at 850°C for 3000 hours was studied. The intergranular borides in that sample were also found to coarsen as in the case of the crept sample. Although the borides from the annealed sample are relatively coarse compared to those in the heat-treated condition, with an average size of  $720\pm 290$  nm (105 borides measured), they are still smaller compared to those after creep deformation. The microstructural evolution of the MC carbides is not considered here, since it has been investigated in a different study showing that intergranular MC carbides can decompose and lead to the formation of  $\eta$  phase [15]. Note that Figures 1a, 1c and 1d are taken at the same magnification to make the extent of coarsening of the borides readily apparent, and that details of the size distribution are provided in supplementary materials as histograms. It should be noted that there was no difference in the precipitate distributions

on transverse and longitudinal (with respect to the applied stress direction) grain boundaries and precipitate free zones (PFZ) were not observed in any of the conditions.

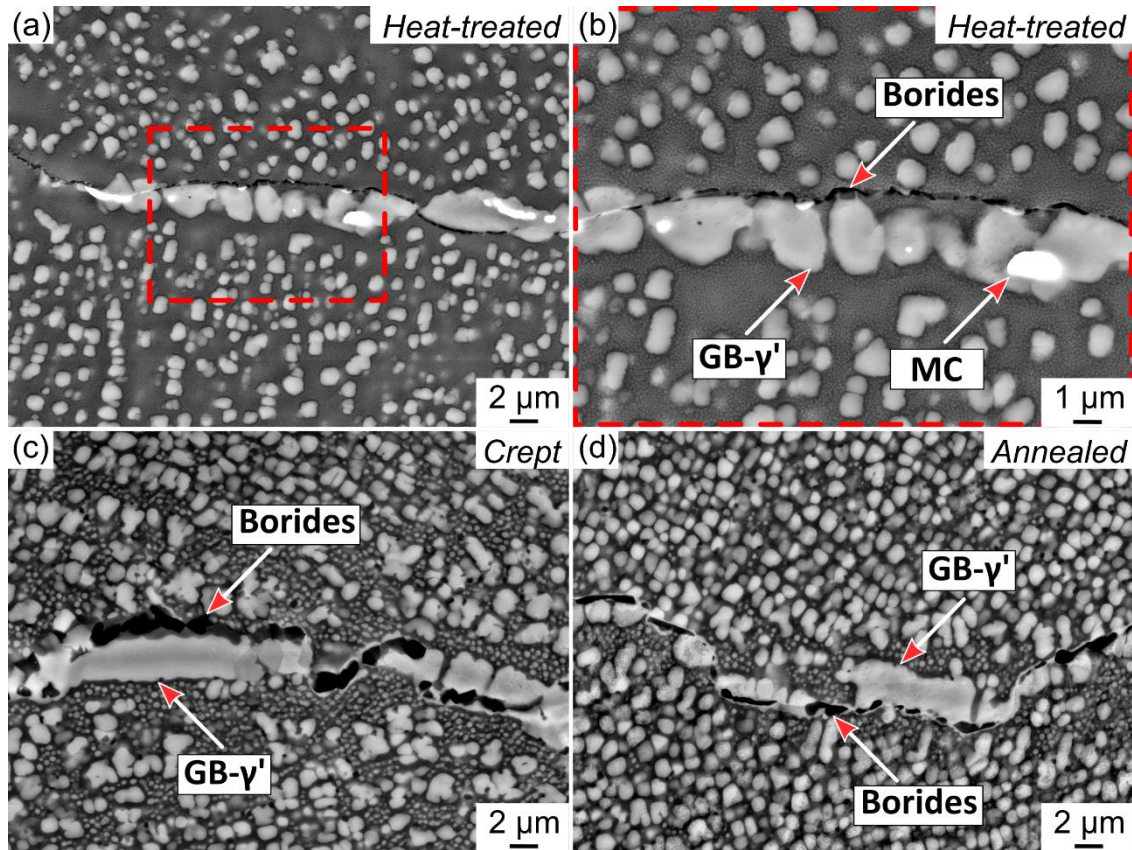


Figure 1: Backscattered electron micrographs of STAL15-CC alloy after: a-b) full heat treatment, c) creep deformation at 850°C/185 MPa up to fracture and d) static annealing at 850°C for 3000 hours.

Our SEM observations show that the coarsening of the boride is enhanced by the externally applied stress, as the borides are larger in the crept sample than in the annealed one. Bulk diffusion of elements from longitudinal to transverse grain boundaries, i.e. Nabarro-Herring creep, is not expected to contribute significantly due to the large grain size of approximately 750μm in average (diffusion path-length) and low homologous temperature of 0.58 [26,27]. In addition, Coble creep would also be unlikely due to the high population of various grain boundary precipitates, such as MC carbides, which would slow down the elemental diffusion [28]. The applied stress can affect the effective diffusivity of atoms, thereby affecting the coarsening rates of the microstructural constituents during creep [29,30]. Even so, the large grain size of the alloy would make contributions from dislocation creep more significant than those from diffusion creep [31,32], as regards to grain boundary precipitation. As such, a possible explanation related to the coarser borides after creep, could be

related to the higher amounts of solutes at grain boundary regions brought by the dislocations following the pipe diffusion mechanism [33]. Indeed, observations of the microstructural evolution of a deformed superalloy have shown indirect evidence that Cr diffusion through dislocations can be faster than via the lattice [34]. However, further investigation is required in order to understand the exact contribution of each mechanism to the coarsening rate of the borides.

The coarsening rate may thus be a life limiting parameter for polycrystalline superalloys with borides. Agglomeration of borides at grain boundaries forming a continuous film can potentially act as crack initiation sites, particularly at grain boundaries transverse to the applied stress during creep. This particular alloy has indeed been shown to be very sensitive to grain boundary cracking, and so the coarsening of borides may limit the creep properties of the alloy, in spite of the  $\gamma/\gamma'$  microstructure, with conventional  $\gamma'$  volume fraction, displaying traditionally good creep resistance [2,14,15,35]. This is similar to what was found before in the case of intergranular  $M_{23}C_6$  carbides in superalloys [36]. The continuous coarsening will leach elements from the surrounding matrix, possibly leading to chemical and microstructural destabilization, and changes in  $\gamma/\gamma'$  equilibrium. It has been previously shown that in the case of STAL15-CC alloy at the vicinity of coarsened borides there is a region depleted of secondary  $\gamma'$  precipitates [15]. Hence, the combination of a continuous film of borides at grain boundaries with regions depleted of secondary  $\gamma'$  precipitates can potentially facilitate the formation of micro cracks. Details of the coarsened borides are therefore investigated next.

### 3.2. Structural information and crystal defects of coarsened borides at 850°C

TEM samples with coarsened borides were investigated for both crept and annealed conditions. Figure 2a shows a HAADF image from a grain boundary of the crept sample. Note that the TEM specimen was prepared along the grain boundary. The  $\gamma$  matrix and  $\gamma'$  precipitates are evidenced, along with several precipitates. Grain boundary borides, identified by their diffraction patterns, are adjacent to each other, and contain planar features. MC carbides are also identified (see green arrow in Figure 2a). Some of the large borides were characterized in more details. A TEM bright field image at higher magnification of an  $M_2B$  boride, indicated by the red box in Figure 2a, is shown in Figure 2b. The diffraction pattern collected from this boride is shown as an inset in Figure 2b, and corresponds to a [111] zone axis of the tetragonal I4/mcm structure, with lattice parameters  $a=0.52$  nm and  $c=0.43$  nm, as reported in the literature [8,37,38]. One can note that this diffraction pattern is very close to that of a [001] zone axis of the Fddd orthorhombic structure of  $M_2B$ , as some  $d_{hkl}$

distances are only 0.02 Å apart. Elongated streaks are visible, which indicate the signature of faulted planes in the {110} planes [39,40]. A high resolution TEM image of boride of Figure 2b is given in Figure 2c, evidencing more clearly the {110} faulted planes obtained after creep deformation at 850°C, in good agreement with the literature [8,37,38]. Finally, a dislocation (the image is rotated compared to Figure 2c to bring the (1-10) planes horizontal) is evidenced in Figure 2d, with an extended strain field. Its Burgers vector was partly determined following the Burgers circuit of Figure 2e. With the assumption that the defect is a perfect dislocation, the Burgers vector is  $\pm 1/2[1-11]$ . The slip plane containing the Burgers vector and the dislocation line is therefore (10-1).

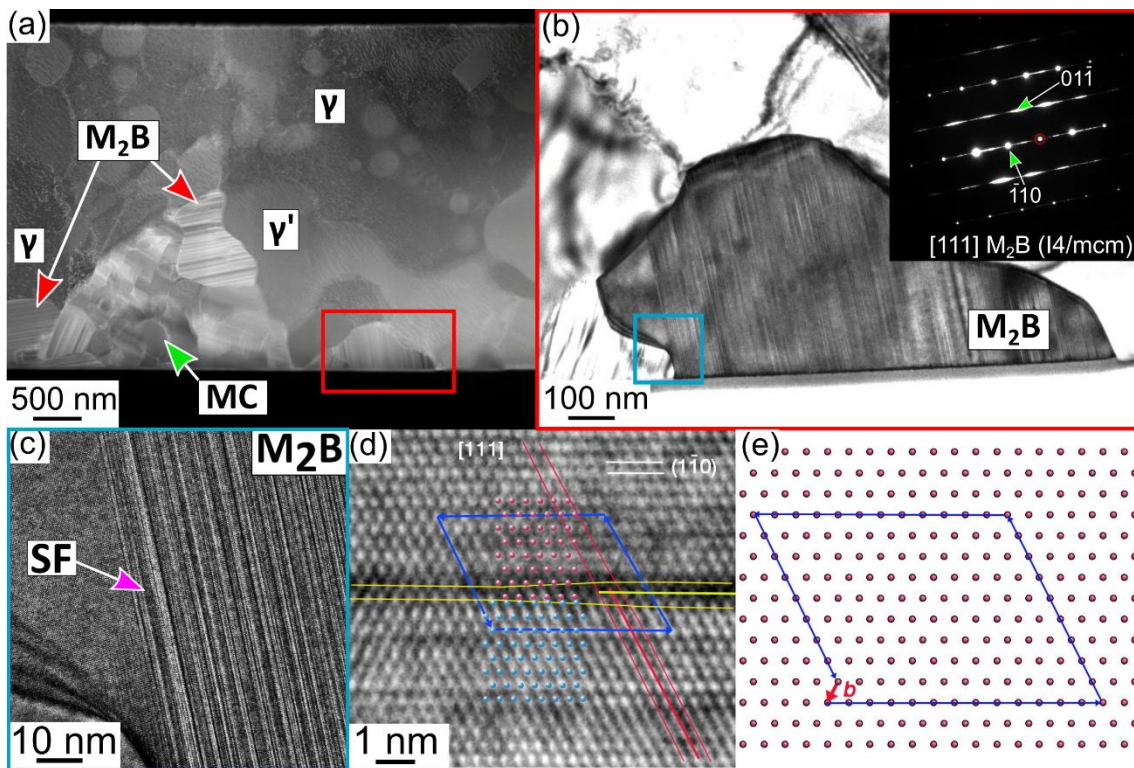


Figure 2: TEM analysis of an intergranular  $M_2B$  boride from the crept sample at 850°C. (a) TEM HAADF image of the sample showing several intergranular  $M_2B$  borides (see red arrows for instance) and an MC carbide (green arrow) along the grain boundary. (b) TEM bright field image of the boride denoted by the blue box in Figure 2b alongside with its diffraction pattern. (c) High resolution TEM image showing details of the faulted planes in the boride from Figure 2b. (d) Image of a dislocation in the boride and (e) corresponding Burgers circuit.

The investigation of another coarsened boride from the crept sample is summarized in Figure 3. Once again, the boride contains a high density of faulted planes. Its diffraction pattern can be indexed with the orthorhombic structure Fddd, with lattice parameters  $a=0.42$  nm,  $b=0.73$  nm and  $c=1.46$  nm. The diffraction pattern given in the inset of Figure 3a shows streaks suggesting that the planar faults are

in the (002) planes. The high resolution TEM image in Figure 3b along with the provided modelling (simulation and overlaid atomic structure, see higher magnification in Figure 3c) of the Fddd structure shows indeed the stacking of (002) planes, with a fault. However, some of the planar features observed in the boride of Figure 3a may also correspond to a change in the crystallographic structure, as shown in Figure 3d. The high-resolution TEM image of this area, from the boride shown in Figure 3a, clearly shows the two structures, Fddd and I4/mcm, successively stacked on top of each other, with the relationship  $[110]_{\text{Fddd}} // [001]_{\text{I4/mcm}}$ .

Overall, the faulted planes in the borides can be identified as normal faulted plane or a change of the crystallographic structure, with these possibilities coexisting in a single precipitate.

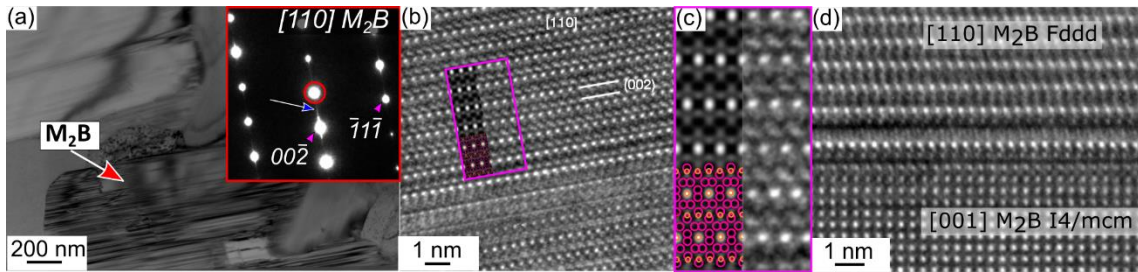
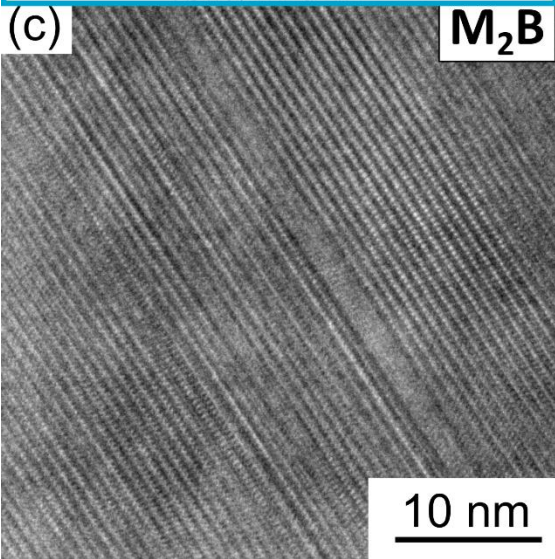
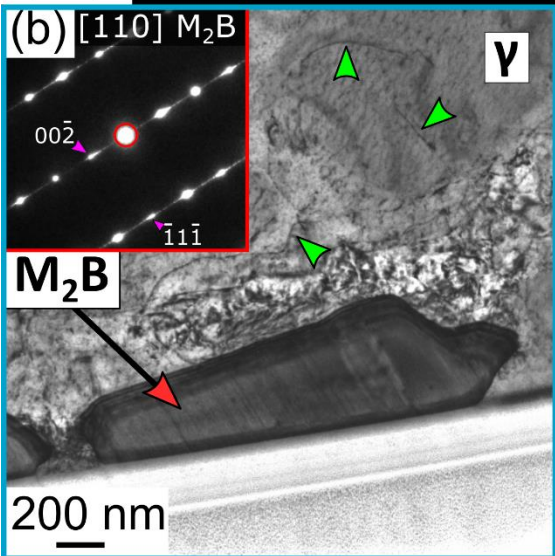
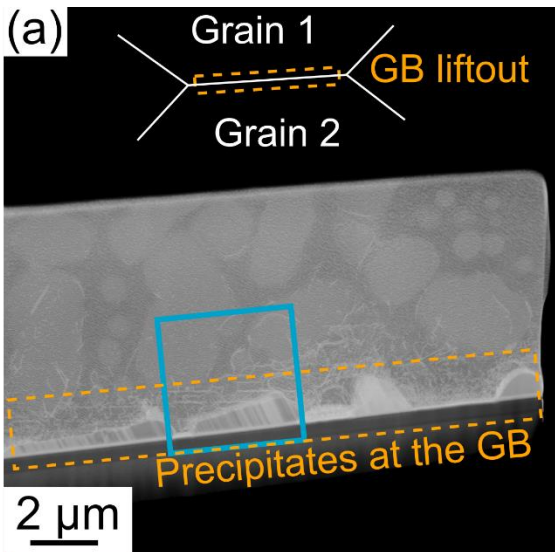


Figure 3: TEM analysis of an intergranular  $M_2B$  boride from the crept sample at  $850^\circ\text{C}$ . (a) TEM bright field image of the boride along with its diffraction pattern. (b) High resolution TEM image of the boride in (a) showing details of the faulted planes in the boride, along with image simulation. In the superimposed structure, Cr atoms are in pink and B atoms in orange. The white dots correspond to B columns (defocus  $-56\text{ nm}$ , thickness  $20\text{ nm}$ ). (c) Higher magnification of the simulation and the observed structure (purple box in (b)). (d) High resolution TEM image of the boride in (a) showing two  $M_2B$  structures, Fddd and I4/mcm stacked on top of each other.

In the case of the annealed sample at  $850^\circ\text{C}$  for 3000 hours (without applying any external stress), similar observations were performed within the coarsened borides. Figure 4a is an HAADF image of a TEM sample taken along a grain boundary containing coarsened  $M_2B$  borides. Figure 4b clearly shows that coarsened borides within the annealed sample are heavily faulted and these planar faults within the  $M_2B$  borides are not the result of deformation under external load. A diffraction pattern taken from the boride in Figure 4b allows to characterize a  $M_2B$  boride exhibiting the Fddd crystal structure in  $[110]$  zone axis, and the streaks in the diffraction pattern (in the same zone axis than the boride of Figure 3) also characterize faults in the (002) planes, evidenced in Figure 4c. Some dislocations are also visible inside the matrix, in the vicinity of the coarsened boride (see green triangles in Figure 4b).



*Figure 4: TEM analysis of an intergranular  $M_2B$  boride from the sample annealed for 3000 hrs at 850°C without load. (a) Schematic of the GB lift-out and TEM HAADF image of the lamella, showing precipitates along the grain boundary (orange dashed rectangle). (b) TEM HAADF image of the area denoted by the blue box in Figure 4a, showing a higher magnification of a boride, and the corresponding diffraction pattern. Green arrows point at dislocations in the neighboring  $\gamma$  matrix. (c) High resolution TEM image of the faulted planes of the borides in (b).*

Overall, the coarsened borides exhibit a tetragonal structure with space group I4/mcm or an orthorhombic one with space group Fddd. They are always heavily faulted, with planar faults in their {110} planes (tetragonal structure) or in their (002) planes (orthorhombic structure). Such faults have been reported before [8,9,37,38], and some can be related to the intergrowth of the two structures, tetragonal and orthorhombic, for which two possible orientation relationships have been reported:  $[001]_{\text{tetragonal}}//[100]_{\text{orthorhombic}}$  and  $(110)_{\text{tetragonal}}//(001)_{\text{orthorhombic}}$  (or normal intergrowth) on one side, and  $[001]_{\text{tetragonal}}//[110]_{\text{orthorhombic}}$  and  $(110)_{\text{tetragonal}}//(001)_{\text{orthorhombic}}$  (or twin-mediated intergrowth) on the other side [8,38]. The case of intergrowth of these two structures is indeed observed in the present case (figure 3). As mentioned by Goldfarb et al. [37], the two structures are actually very close, since only a slight adjustment of B atoms lying on the {110} atomic planes is needed to transform the  $Cr_2B$  structure from I4/mcm to Fddd. Besides, they share the same building polyhedron, as evidenced by Hu et al. [8].

### **3.3. Interactions of solutes with planar defects in borides**

APT specimens were prepared from both crept and annealed specimens, aiming to investigate interactions of solutes with the planar faults taking place during the coarsening of the borides.

Figure 5a shows an APT reconstruction from a coarsened intergranular boride from the crept sample. A 2D density map of Cr in Figure 5b, corresponding to the area denoted by the rectangle in Figure 5a, reveals the presence of compositional variations along planes that cross the entire boride. Due to the angle between the planes and the needle-shaped specimen's evaporation axis Z, the possibility that these planes correspond to a field evaporation artefact can be disregarded.

A 1D composition profile was extracted from an elliptical cylindrical region of interest taken along the arrow #1 in Figure 5b, is shown in Figure 5c. Composition fluctuation of Cr and B can be seen, where Cr decreases in regions where B increases. In particular, five B-rich regions were identified, with B enrichment varying from region to region between 25.0 and 28.0 at.%. The lower B-content characterized here compared to the expected stoichiometry of  $M_2B$  can be explained by the detector

dead-time, and was already reported for boron [41], similarly to results on nitrogen, oxygen and carbon [42,43]. Besides the enrichment of B on planar features, partitioning at dislocations was also observed: tubular features, which correspond to elemental segregation at dislocations, also appear within the APT reconstruction in Figure 5a. This is investigated in more details in the next section.

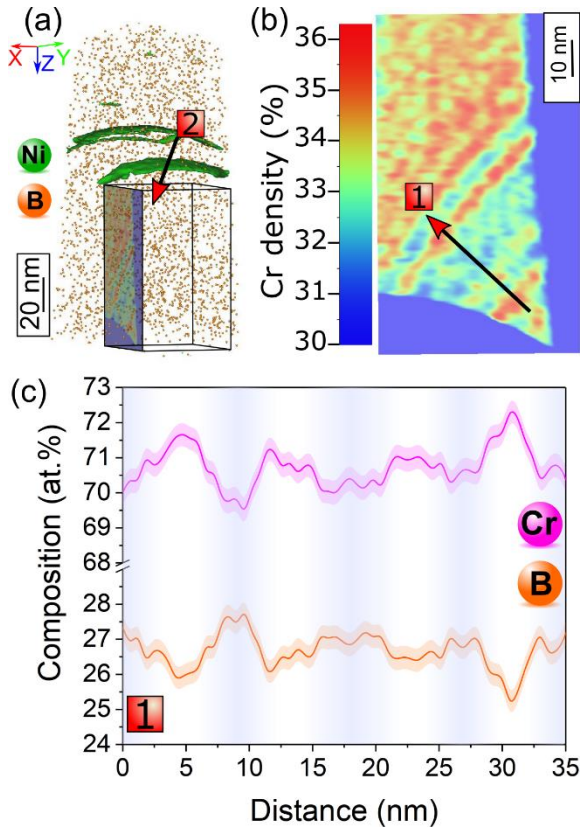


Figure 5: APT analysis of an intergranular  $M_2B$  boride from the crept sample at 850°C. (a) Atom probe reconstruction from the boride containing dislocations highlighted by iso-composition surfaces of 0.8 at.% Ni. The composition profile corresponding to the arrow #2 is studied in greater details in Figure 7a. (b) 2D density map for Cr from the box in Figure 5a. (c) 1D concentration profile across the B-rich planes indicated by the arrow #1 in Figure 5b. The B-rich planes are highlighted by a blue background area.

APT analysis was also performed for intergranular coarsened borides from the annealed sample at 850°C containing planar faults. Figure 6a shows an APT reconstruction containing a boride and its interface with the  $\gamma$  matrix. Planar fluctuations of Cr are observed as shown in the 2D compositional map in Figure 6b, extracted from the region indicated by the black dashed box in Figure 6a. A 1D-composition profile across the planar compositional variations as denoted by the arrow #1 in Figure 6a, is plotted in Figure 6c. As in the crept sample, B-rich planes (highlighted by a blue background)

are also observed within the boride of the annealed sample. These observed planar B-enrichments are concurrent with Cr depletions.

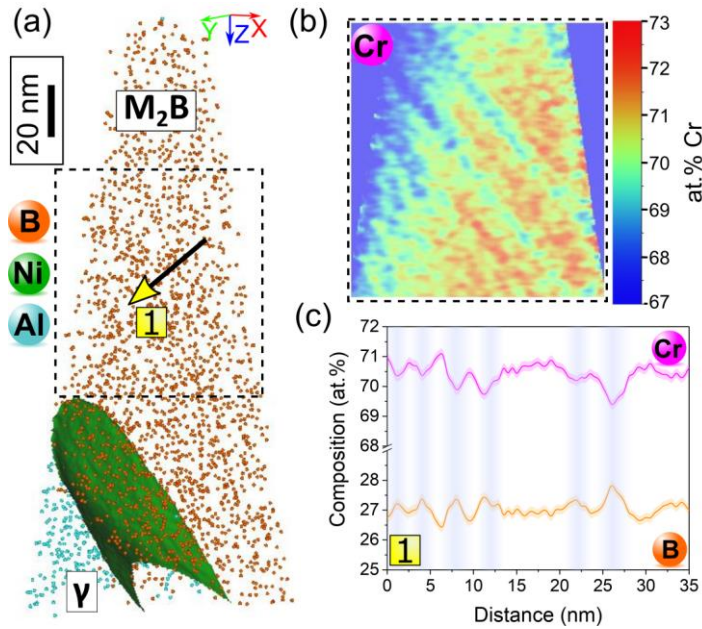


Figure 6: APT analysis of an intergranular  $M_2B$  boride from the annealed sample at  $850^\circ\text{C}$ . (a) Atom probe reconstruction from the boride and its interface with the  $\gamma$  matrix. The interface is shown with an iso-composition surface at 10 at.% Ni. (b) 2D concentration map for Cr corresponding to the black dashed boxed region in 6a. (c) 1D concentration profiles along the yellow arrow #1 in 6a for Cr and B.

The numerous B-rich planes are likely to be correlated to the planar faults or structural changes in the  $\{110\}_{I4/mcm}$  planes or the  $(002)_{Fdd}$  planes characterized by TEM in the coarsened  $M_2B$  borides. Although the formation of deformation induced stacking faults in MB-type borides has been previously reported [44], based on the present results, it seems that the present planar faults are not mechanically induced, since they are also observed in the case of the annealed sample, with no external load. The high density of faults would then be a consequence of growth defects, with variations of the stacking sequence that lead to the introduction of a fault or of another structure, that extends across the whole precipitate.

The intergrowth of tetragonal and orthorhombic  $M_2B$  is expected to be neutral from a composition point of view. Published electron energy loss spectroscopy (EELS) measurements reported a homogeneous distribution of B and Cr across the faults [38], but the length over which the composition was measured by EELS is very large (600 nm), and this would not have been able to resolve the small, local variations that APT was able to unveil in this study, in the range of about ten

nm and of a few at.%. A hypothesis to explain the compositional changes, becoming off-stoichiometry, could be that the stacking of the building polyhedron leads to the local formation to another phase with different stoichiometry, such as  $M_5B_3$  or  $M_3B_2$ . Intergrowth of these last two structures has been reported before, and the  $M_5B_3$  structure contains building polyhedron of  $M_2B$  [45]. Moreover, layers of  $M_2B$  in  $M_5B_3$  have been observed [45]. However, such intergrowth occurs in the tetragonal  $\langle 001 \rangle$  direction, and the orientation relationships found in the present study would rather suggest growth along the  $\langle 110 \rangle_{I4/mcm} / \langle 001 \rangle_{Fddd}$  direction. Besides, HRTEM could not evidence the presence of  $M_5B_3$  or  $M_3B_2$  in the present case. Another possibility would be that there is occasionally a loss of symmetry of the Fddd structure, that would accommodate non-stoichiometric compositions, as observed in  $M_2B$  borides of Co-Re-Cr superalloys [46]. Reaching locally such non-stoichiometric states, possibly influencing the crystal structure, may be due to different diffusion rates between Cr and B, leading to lesser available amounts of one of the solutes with respect to the other. However, in order to fully interpret the complex compositional fluctuations of B and Cr that are reported here, more systematic structural and compositional investigations are required at various temperatures and particularly in the early stages of coarsening of the borides.

### 3.4. Partitioning of solutes at dislocations in deformed borides

Finally, investigations at the dislocations observed only in the crept borides, and their interactions with solutes, were performed. Figure 5a shows dislocations highlighted by a Ni-isocomposition surface. A 1D composition profile, extracted from a cylindrical region of interest perpendicular to the dislocation indicated by the arrow #2 in Figure 5a is plotted in Figure 7a. An enrichment of Ni and Co at the dislocation up to approximately 4 and 2 at.% is revealed, respectively, alongside a concurrent depletion of B and Cr.

Figure 7b shows a second APT 3D-reconstruction from a coarsened intergranular boride from the crept sample. Similar Ni- and Co-rich dislocations as those reported in Figure 5 and Figure 7a, regarding the segregation behavior, are observed. In this case, the dislocations appear to be in two different crystallographic planes, however this needs to be confirmed by further TEM investigations. Figure 7c shows a close-up on the region-of-interest indicated by the black rectangle in Figure 7b. A 2D composition map is plotted for Ni across the dislocation revealing two maxima and suggesting that this dislocation is a pair of dislocations within the boride. A composition profile is extracted from an elliptical cylinder region of interest across the dislocation, along the red arrow #3 (Figure 7c), and is displayed in Figure 7d. It confirms that two distinct dislocations are observed, enriched in Ni and

Co, as for the dislocation in Figure 5, with contents up to 4.4 at.% and 2.6 at.%, respectively. Boron and chromium seem again to be depleted at the dislocation.

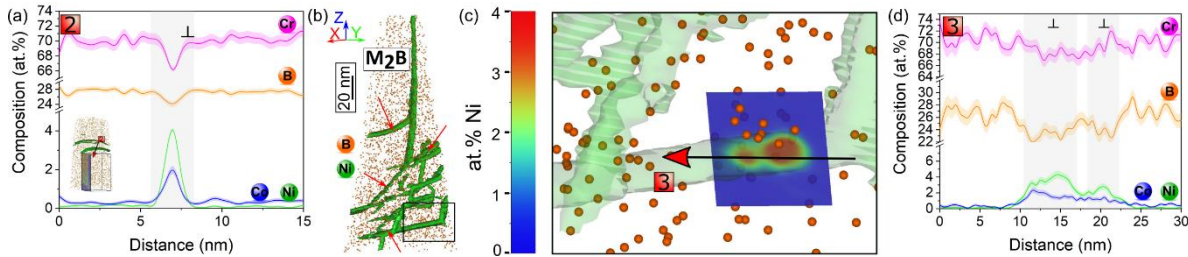


Figure 7: (a) 1D composition profile across the dislocation in Figure 5a, along the arrow #2 (see inset), showing an increase of Ni and Co at the dislocation. Error bars are shown as lines filled with color and correspond to the  $2\sigma$  counting error. (b)-(d) APT analysis of an other intergranular  $M_2B$  boride from the crept sample at 850°C. (b) Atom probe reconstruction from the boride. Dislocations, highlighted by iso-composition surfaces of 1.0 at.% Ni., are denoted by red arrows. (c) Magnified view of the APT reconstruction from the rectangle 1 in Figure 7b, with a 2D concentration map plotted across a dislocation for Ni. (d) 1D concentration profiles across the dislocation indicated by the red arrow in Figure 7c. Error bars are shown as lines filled with color and correspond to the  $2\sigma$  counting error.

Although TEM imaging of the dislocations was uneasy due to the high density of planar faults, the present APT results, coming from two different datasets obtained from distinct samples and from different locations, allow us to suggest that it is not an isolated observation. Imaging dislocations in the APT datasets is enabled by the observed partitioning of Ni and Co at the dislocations. The measured partitioning, with compositions as high as approximately 4.0 and 2.0 at.%, respectively, is substantial considering that their base compositions are below 0.2 at.% for Ni and 0.5 at.% for Co within the boride. An extended core, as the one characterized by TEM in Figures 2d and 2e, could also accommodate large amounts of solutes. Partition of solutes at defects, such as dislocations, is driven by the minimization of the system's free energy. This can lead to either conventional Cottrell- or Suzuki-type decoration or even to spatially confined linear chemical-structural transformation states [47,48]. Both effects can be seen as akin to a partitioning phenomenon between the boride matrix and the defect and hence depend on the composition of the borides as well as of the surrounding phases in contact with the dislocations [49]. In both cases reported here, Ni and Co partition to the dislocations, while the concentrations of those two solutes within the borides are low, especially compared to their concentration in the  $\gamma$  matrix (see [15]). Therefore, it is suggested that the observed solutes partitioning at the dislocations have most likely diffused along the dislocations line connected to the matrix via pipe diffusion rather than having been collected during the dislocation glide inside the boride. One could argue that some of the observed dislocations are related to the

misfit between the structures involved in the coarsening. However, stacking of tetragonal and orthorhombic  $M_2B$  has been reported to lead to coherent interfaces, without lattice misfit dislocations [8].

Therefore, the present results rather suggest that the observed defects are deformation-induced dislocations. Significant plasticity in borides deformed in the same temperature range has also been observed and interpreted by the nature of chemical bonding [50]. This could indicate that the local stresses built up on the interfaces during creep can be released by the plastic deformation of boride particles, which could improve the creep resistance. However, this needs to be further explored by investigating the deformation of borides at various creep conditions.

#### **4. Conclusions**

The partitioning of solutes at crystal defects at intergranular Cr-rich  $M_2B$  borides as a result of their microstructural evolution under creep and annealing was studied for the polycrystalline nickel-based superalloy STAL15-CC. The following conclusions can be drawn:

- Borides were found to coarsen during creep deformation at 850°C/185MPa after approximately 3000 h and during static annealing at 850°C for 3000 h. Borides are coarser after creep compared to after annealing (1060 nm and 720 nm in average, respectively).
- $M_2B$  borides are characterized, with tetragonal  $I4/mcm$  or orthorhombic  $Fddd$  structure. The coarsened borides, both after creep and annealing, display a high density of faulted planes in the  $\{110\}$  planes (tetragonal structure) or in the (002) planes (orthorhombic). Intergrowth of both structures is also reported.
- Planar fluctuations of B and Cr were characterized by APT. It is believed that they are related to the observed planar faults or to the structural changes due to the intergrowth.
- Enrichment of Ni and Co up to 6.1 and 2.4 at.%, respectively, was measured by APT at the dislocations within the borides of the crept sample. The solute partition at the dislocation is believed to be related to pipe diffusion of solutes from the surrounding matrix, leading to potential alterations of the latter's composition.

#### **Declaration of Competing Interest**

The authors declare that they have no known competing financial interests or personal relationships that could have appeared to influence the work reported in this paper.

## Acknowledgements

P.K. thanks Siemens Industrial Turbomachinery for provision of the material and performing the creep and annealing tests. Uwe Tezins & Andreas Sturm for their support to the FIB & APT facilities at MPIE. L.L. thanks P. Vermaut for fruitful discussions. We are grateful for the financial support from the Max-Planck Gesellschaft via the Laplace project for both equipment and personnel (P.K.). BG acknowledges financial support from the ERC-CoG-SHINE-771602. Authors also acknowledge use of the ZGH infrastructure (FIB Thermo Fisher Scientific, Helios G4 CX).

## References

1. M. Kolb, L. P. Freund, F. Fischer, I. Povstugar, S. K. Makineni, B. Gault, D. Raabe, J. Müller, E. Spiecker, S. Neumeier, and M. Göken, *Acta Materialia* **145**, 247 (2018).
2. P. Kontis, H. A. M. Yusof, S. Pedrazzini, M. Danaie, K. L. Moore, P. A. J. Bagot, M. P. Moody, C. R. M. Grovenor, and R. C. Reed, *Acta Materialia* **103**, 688 (2016).
3. D. Tytko, P.-P. Choi, J. Klöwer, A. Kostka, G. Inden, and D. Raabe, *Acta Materialia* **60**, 1731 (2012).
4. T. Alam, P. J. Felfer, M. Chaturvedi, L. T. Stephenson, M. R. Kilburn, and J. M. Cairney, *Metallurgical and Materials Transactions A* **43**, 2183 (2012).
5. X. B. Hu, H. Y. Niu, X. L. Ma, A. R. Oganov, C. A. J. Fisher, N. C. Sheng, J. D. Liu, T. Jin, X. F. Sun, J. F. Liu, and Y. Ikuhara, *Acta Materialia* **149**, 274 (2018).
6. P. A. J. Bagot, O. B. W. Silk, J. O. Douglas, S. Pedrazzini, D. J. Crudden, T. L. Martin, M. C. Hardy, M. P. Moody, and R. C. Reed, *Acta Materialia* **125**, 156 (2017).
7. M. Thuvander and K. Stiller, *Materials Science and Engineering: A* **281**, 96 (2000).
8. X. B. Hu, Y. L. Zhu, and X. L. Ma, *Acta Materialia* **68**, 70 (2014).
9. H. R. Zhang, O. A. Ojo, and M. C. Chaturvedi, *Scripta Materialia* **58**, 167 (2008).
10. M. J. Kaufman and V. I. Levit, *Philosophical Magazine Letters* **88**, 259 (2008).
11. T. J. Garosshen, T. D. Tillman, and G. P. McCarthy, *Metallurgical Transactions A* **18**, 69 (1987).
12. L. Xiao, M. C. Chaturvedi, and D. Chen, *Journal of Materials Engineering and Performance* **14**, 528 (2005).
13. B. C. Yan, J. Zhang, and L. H. Lou, *Materials Science and Engineering: A* **474**, 39 (2008).
14. P. Kontis, E. Alabort, D. Barba, D. M. Collins, A. J. Wilkinson, and R. C. Reed, *Acta Materialia* **124**, 489 (2017).
15. P. Kontis, A. Kostka, D. Raabe, and B. Gault, *Acta Materialia* **166**, 158 (2019).
16. H. L. Ge, J. D. Liu, S. J. Zheng, Y. T. Zhou, Q. Q. Jin, X. H. Shao, B. Zhang, Y. Z. Zhou, and X. L. Ma, *Materials Letters* **235**, 232 (2019).
17. R. R. Unocic, N. Zhou, L. Kovarik, C. Shen, Y. Wang, and M. J. Mills, *Acta Materialia* **59**, 7325 (2011).
18. K. Shinagawa, T. Omori, K. Oikawa, R. Kainuma, and K. Ishida, *Scripta Materialia* **61**, 612 (2009).
19. E. Cadel, D. Lemarchand, S. Chambrelaud, and D. Blavette, *Acta Materialia* **50**, 957 (2002).
20. Y. S. Zhao, J. Zhang, Y. S. Luo, B. Zhang, G. Sha, L. F. Li, D. Z. Tang, and Q. Feng, *Acta Materialia* **176**, 109 (2019).
21. P. Kontis, *Scripta Materialia* **194**, 113626 (2021).
22. L. Lilensten, S. Antonov, B. Gault, S. Tin, and P. Kontis, *Acta Materialia* **202**, 232 (2021).

23. K. Roar, *MacTempas* (n.d.).
24. K. Thompson, D. Lawrence, D. J. Larson, J. D. Olson, T. F. Kelly, and B. Gorman, *Ultramicroscopy* **107**, 131 (2007).
25. R. C. Reed, A. C. Yeh, S. Tin, S. S. Babu, and M. K. Miller, *Scripta Materialia* **51**, 327 (2004).
26. F. R. N. Nabarro, *Phys. Soc. Lond.* **75** (1948).
27. C. Herring, *Scripta Metallurgica* **5**, 273 (1971).
28. R. L. Coble, *Journal of Applied Physics* **34**, 1679 (1963).
29. S. V. Prikhodko and A. J. Ardell, *Acta Materialia* **51**, 5001 (2003).
30. A. J. Ardell and S. V. Prikhodko, *Acta Materialia* **51**, 5013 (2003).
31. J. K. Tien and R. P. Gamble, *Metallurgical Transactions* **2**, 1663 (1971).
32. H. Choe and D. C. Dunand, *Materials Science and Engineering: A* **384**, 184 (2004).
33. P. Kontis, D. M. Collins, A. J. Wilkinson, R. C. Reed, D. Raabe, and B. Gault, *Scripta Materialia* **147**, 59 (2018).
34. S. Antonov, B. Li, B. Gault, and Q. Tan, *Scripta Materialia* **186**, 208 (2020).
35. W. D. Summers, E. Alabort, P. Kontis, F. Hofmann, and R. C. Reed, *Materials at High Temperatures* **33**, 338 (2016).
36. X. Z. Qin, J. T. Guo, C. Yuan, C. L. Chen, and H. Q. Ye, *Metallurgical and Materials Transactions A* **38**, 3014 (2007).
37. I. Goldfarb, W. D. Kaplan, S. Ariely, and M. Bamberger, *Philosophical Magazine A* **72**, 963 (1995).
38. X. B. Hu, Y. L. Zhu, X. H. Shao, H. Y. Niu, L. Z. Zhou, and X. L. Ma, *Acta Materialia* **100**, 64 (2015).
39. A. G. Fitzgerald and M. Mannami, *Proceedings of the Royal Society of London. Series A, Mathematical and Physical Sciences* **293**, 169 (1966).
40. M. J. Whelan and P. B. Hirsch, *The Philosophical Magazine: A Journal of Theoretical Experimental and Applied Physics* **2**, 1121 (1957).
41. F. Meisenkothen, E. B. Steel, T. J. Prosa, K. T. Henry, and R. [Prakash Kolli, *Ultramicroscopy* **159**, 101 (2015).
42. B. Gault, D. W. Saxey, M. W. Ashton, S. B. Sinnott, A. N. Chiaramonti, M. P. Moody, and D. K. Schreiber, *New Journal of Physics* **18**, 033031 (2016).
43. Z. Peng, F. Vurpillot, P.-P. Choi, Y. Li, D. Raabe, and B. Gault, *Ultramicroscopy* **189**, 54 (2018).
44. B. Jiang, C. Chen, X. Wang, H. Wang, W. Wang, H. Ye, and K. Du, *Acta Materialia* **165**, 459 (2019).
45. X. B. Hu, Y. L. Zhu, N. C. Sheng, and X. L. Ma, *Scientific Reports* **4**, 7367 (2014).
46. M. C. Paulisch, N. Wanderka, G. Miehe, D. Mukherji, J. Rösler, and J. Banhart, *Journal of Alloys and Compounds* **569**, 82 (2013).
47. A. K. da Silva, G. Leyson, M. Kuzmina, D. Ponge, M. Herbig, S. Sandlöbes, B. Gault, J. Neugebauer, and D. Raabe, *Acta Materialia* **124**, 305 (2017).
48. M. Kuzmina, M. Herbig, D. Ponge, S. Sandlöbes, and D. Raabe, *Science* **349**, 1080 (2015).
49. X. Wu, S. K. Makineni, P. Kontis, G. Dehm, D. Raabe, B. Gault, and G. Eggeler, *Materialia* **4**, 109 (2018).
50. S. Lartigue-Korinek, M. Walls, N. Haneche, L. Cha, L. Mazerolles, and F. Bonnet, *Acta Materialia* **98**, 297 (2015).